IEEE Access
Multidisciplinary | Rapid Review | Open Access Journal

IEEE GEOSCIENCE AND REMOTE SENSING SOCIETY SECTION

Received 15 October 2024, accepted 5 November 2024, date of publication 18 November 2024, date of current version 27 November 2024.

Digital Object Identifier 10.1109/ACCESS.2024.3501279

RESEARCH ARTICLE

Modeling Marine Geoid in the China Seas and Its Adjacent Ocean Based on Satellite Altimeter-Derived Gravity Anomaly Model

HUIYING ZHANG[1], XIN LIU[1], ZHEN LI[1], XIAOTAO CHANG[2], HEPING SUN[3], HUI LI[4], AND JINYUN GUO[1]

[1]College of Geodesy and Geomatics, Shandong University of Science and Technology, Qingdao, Shandong 266590, China
[2]Land Satellite Remote Sensing Application Center, Ministry of Natural Resources, Beijing 100048, China
[3]Innovation Academy for Precision Measurement Science and Technology, Chinese Academy of Sciences, Wuhan 430077, China
[4]School of Marine Science and Technology, Northwestern Polytechnical University, Xi'an 710072, China

Corresponding author: Xin Liu (xinliu1969@126.com)

This work was supported by the National Natural Science Foundation of China under Grant 42274006, Grant 42174041, and Grant 42192535.

ABSTRACT The marine geoid can be determined through the utilization of the marine gravity anomaly model. The accuracy of retrieving marine gravity anomaly model with altimetry data has been improved due to the abundance and high quality of available altimetry data. The SDUST2022 GRA marine gravity anomaly model is the global marine gravity anomaly model constructed by integrating multi-source altimeter satellites, including ICEsat-2 laser altimeter satellite for the first time. The model optimizes the deflection of the vertical accuracy imbalance. The Stokes formula is employed in this study to construct the geoid model, while the two-dimensional fast Fourier transform convolution in planar coordinate is utilized to enhance computational efficiency. Additionally, the remove-computer-restore method is applied during the calculation process. Firstly, the accuracy of the algorithm is verified using the 2190-degree XGM2019e_2159 gravity field model and the 2159-degree EGM2008 gravity field model. Subsequently, the XGM2019e_2159 is removed from the SDUST2022 GRA marine gravity anomaly model, and the residual geoid height is computed utilizing the Stokes formula. Then, the geoid height of the corresponding reference field is restored. Finally, a geoid model for China Sea and its adjacent ocean is constructed. The results showed that the geoid of the China Sea and its adjacent ocean gradually increases from west to east, and the longwave and shortwave characteristics of the seafloor can be clearly seen. The reliability of the model established in this paper was verified by the least-squares collocation method, and the geoid model calculated by the two methods had a good consistency. The mean sea surface model was introduced to calculate the mean dynamic topography. According to the mean dynamic topography, the Kuroshio Extension and the mesoscale eddy phenomenon caused by the instability of background current could be clearly seen. Compared with the mean dynamic topography of DTU22MDT, the difference between the two mean dynamic topography was basically within the range of centimeters. This showed that the mean dynamic topography of the China Sea and its adjacent ocean calculated in this paper was reliable, that is, the geoid of the China Sea and its adjacent ocean constructed in this paper was reliable.

INDEX TERMS China Sea and its adjacent ocean, geoid, least-squares collocation, mean dynamic topography, satellite altimeter-derived marine gravity anomaly model, Stokes formula.

I. INTRODUCTION

The geoid is the gravity equipotential plane closest to the mean sea surface height, and it is the base level of elevation,

The associate editor coordinating the review of this manuscript and approving it for publication was Gerardo Di Martino.

reflecting important information such as the shape of the earth, the structural density of the internal materials, the stress field and the earth's ocean currents [1]. High precision marine geoid is an important basis for ocean mapping, marine science research and understanding of geophysical changes, and it plays a crucial role in studying ocean circulation patterns and ocean current dynamics.

The classical methods for determining the marine geoid include Stokes formula and least-squares collocation (LSC) method. In addition, other methods can also be used to determine the marine geoid, such as the Boundary Element Method (BEM) [2], Poisson Wavelet Radial Basis Function (RBF) method [3], and the least squares collocation method in the frequency domain [4]. Stokes formula is a classical method for integrating gravity anomalies published by Stokes in 1849 [5] and has been used for geoid determination in several continental regions [6], [7], [8], [9], [10], [11]. The Stokes formula, in theory, represents the integral calculation of gravity anomalies distributed continuously on a global scale. However, due to practical limitations, the regional geoid model is predominantly determined by the remove-compute-restore (RCR) techniques. The essence of the RCR is to remove the long-wave gravity field data, the residual component is computed, and the corresponding long-wave gravity field data is restored [12], [13]. In order to enhance the computational efficiency of the Stokes formula, Strang van Hees introduced the fast Fourier transform (FFT) technique in 1990 [14]. After that, The FFT techniques have been extensively employed in the field of physical geodesy, and has become the main method for calculating the approximation of the gravity field [15], [16], [17], [18], [19], [20], [21].

The LSC method has been successfully employed in several regions for geoid determination [22], [23], [24], [25], [26], [27]. The fundamental concept is that, apart from random variables, there exist two sets of random variables known as signal and noise, which are interconnected through a covariance function [28]. The crucial aspect of LSC method is to calculate the covariance function between each physical quantity. Due to the existence of a functional relationship between gravity observations and disturbing potential, once we acquire the covariance function of the disturbing potential, the covariance function between any observation according to the law of covariance propagation can be obtained [29]. The LSC method provides a direct fusion method of multi-source gravity data modeling, which can naturally combine altimetry data, ship-borne data and airborne gravity data [3], [30], [31]. Consequently, in comparison to the Stokes formula, the LSC method entails longer computational time.

The marine geoid research relies on a data foundation of high-precision and high-resolution models of marine gravity anomalies. After the Geodetic mission (GM) data of Geosat and ERS-1 altimeter were fully released in 1995, The marine gravity anomaly model integrating multi-source altimetry satellite data has been studied. With the successful launch of ERS-1's follow-up satellite ERS-2 and the Topex/Poseidon and Jason-1/2 satellites, a global 1'×1' marine gravity anomaly model began to constructed [32]. CryoSat-2 satellite, launched in 2010, provided new and higher-precision observation data for the inversion of marine gravity anomalies [33]. As a near-polar orbit satellite, CryoSat-2 covered almost all sea areas in the world, and could calculate gravity anomalies in polar blank regions. The analysis of the Cryosat-2 satellite indicates that the data exhibits a low level of noise and a high degree of geoid signal identification, therefore it could provide higher resolution shortwave information for the inversion of marine gravity anomaly model [34]. The subsequent GM data of Jason satellites and Saral/Altika satellites had also injected more high-quality altimetry data for the construction of marine gravity anomaly models [35], [36]. HY-2A and its follow-up altimetry satellites launched by China had also made important contributions to the inversion of marine gravity anomalies [37]. With the development of altimetry satellite measurement mode, the altimetry satellite of new measurement mode has been studied. Laser altimetry satellite and wide-swath interferometer satellite had become the development focus of the new generation altimetry satellite. The ICESat-2 laser altimeter satellite, launched in 2018, was evaluated and found that its single trajectory can recover the marine geoid at a wavelength of 20km, similar to the best radar altimeters, and the accuracy of ICESat-2 data in coastal areas surpasses that of coastal data obtained from other radar altimeters [38]. The recently released SDUST2022GRA is the global marine gravity anomaly model that integrates data from ICEsat-2 and other multi-source altimetry satellites for the first time and its spatial resolution can reach 20km in a certain area [39]. The surface water and ocean topography (SWOT) satellite, launched in 2022, could obtain two-dimensional high-resolution surface height in the open ocean, providing two-dimensional marine altimetry data for the construction of marine gravity anomaly models [40]. The sea surface height data of SWOT for the northern South China Sea were simulated, and gravity anomalies within this region were calculated using this dataset [41]. The evaluation results indicate that the high-quality marine gravity anomaly can be obtained from simulated multi-period SWOT data. However, there is no global marine gravity anomaly model that integrates SWOT data.

In this study, based on the RCR method, the correctness of the Stokes formula is validated by utilizing the 2190-degree XGM2019e_2159 and 2159- degree EGM2008 gravity field models. Then, the 2160-degree XGM2019e_2159 gravity anomaly model is removed from the latest marine gravity anomaly model of SDUST2022GRA, and the residual geoid height is computed utilizing two-dimensional FFT (2D FFT) Stokes formula, and then the 2160-degree XGM2019e_2159 reference geoid height is recovered, ultimately resulting in the determination of the geoid model for the China Sea and its adjacent ocean. In order to verify the reliability of the geoid model constructed by Stokes formula, the geoid model constructed by LSC method is used as inspection data for accuracy evaluation. The mean dynamic topography (MDT) of China Sea and its adjacent ocean is calculated

by combining the geoid calculated in this paper with the mean sea surface (MSS) model of SDUST2020 MSS, and the DTU22MDT is selected for comparative study.

II. RESEARCH AREA AND DATA

A. RESEARCH AREA

The selected research area of this paper is China Sea and its adjacent ocean. The China Sea and its adjacent ocean contain the Bohai Sea, Yellow Sea, East China Sea, South China Sea and a number of islands and reefs. This is where the Eurasian, Indo-Australian and the Pacific plates. The intricate geological characteristics of this junction render it an ideal natural laboratory for investigating the phenomena of continental fragmentation and seafloor spreading [42], [43]. In addition, The Kuroshio flow phenomenon exists here. The Kuroshio current transports a significant amount of energy from lower latitudes to higher latitudes, resulting in a complex and dynamic oceanic environment and current patterns within this region. Therefore, this sea area is also the best place to study the dynamic mechanism of the deep ocean [44]. The complex seafloor topography and ocean current movement of the China Sea and its adjacent ocean are of great significance to the study of geoid and the subsequent MDT. The China Sea and its adjacent ocean of 0° ∼ 45°N and 100° ∼ 140°E are used as the research area of this paper, and the marine geoid model of the China Sea and its adjacent ocean is established and the changes of MDT are discussed.

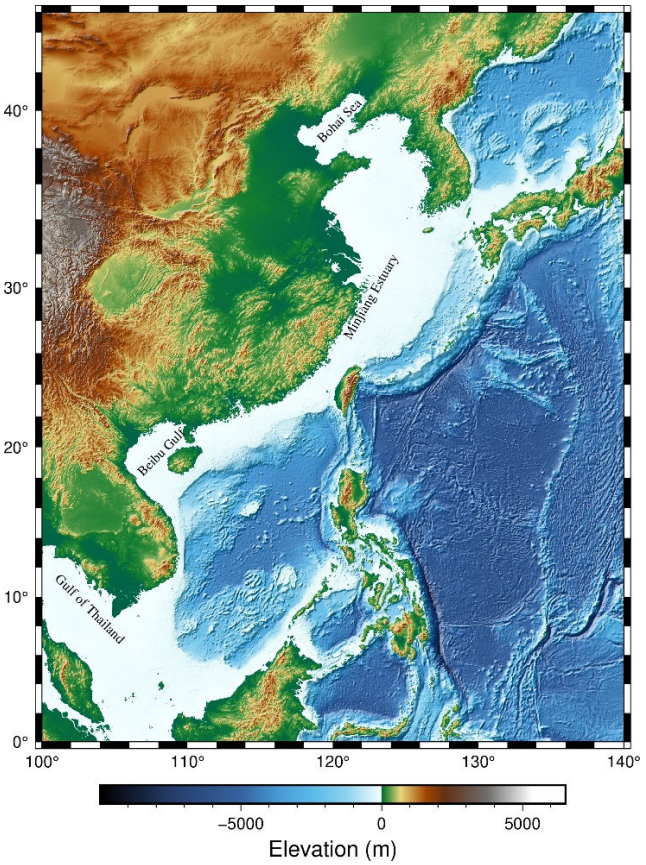

FIGURE 1. China Sea and its adjacent ocean.

B. GLOBAL MARINE GRAVITY ANOMALY MODEL

The global marine gravity anomaly model selected in this paper is SDUST2022GRA model [39]. The SDUST2022GRA model is based on T/P, Jason-1/2, CryoSat-2, SARAL, Sentinel-3A/3B/6A, ICESat-2 and other multi-source altimetry satellite data. It covers 80° north and south latitude and has a grid resolution of 1'×1.' Compared with the marine gravity anomaly models of SIO and DTU series published by international research institutions, this model uses the ICEsat-2 laser altimeter satellite for the first time. ICEsat-2 laser altimeter satellite employs a micropulse multi-beam photon counting radar system for the acquisition of ground information, and uses three simultaneous observation beam groups to collect ground height information, so that the deflection of the vertical along the orbit direction and across the orbit direction can be obtained. This method of observation reduces the imbalance of the deflection of the vertical accuracy caused by only using altimeter data along the track direction [39].

C. REFERENCE GRAVITY FIELD MODEL

The Earth Gravitational Field selected in this paper are the XGM2019e_2159 model [45] and the EGM2008 model [46], both of which are available through the International Centre for Global Earth Models (ICGEM). The XGM2019e_2159 model is a comprehensive global gravity field model with a spherical harmonic expansion degree and order of 5399, providing a spatial resolution of about 2.' It is based on satellite gravity model of GOCO06s, marine gravity anomaly model of DTU13, as well as gravity measurements data of land and ocean [45]. The EGM2008 model is constructed from land, altimetry and airborne gravity data. The degree and order are complete at 2159 and it also includes additional coefficients of degree 2190 and order 2159 [46].

D. MEAN SEA SURFACE (MSS) MODEL

The MSS model used in this paper is the SDUST2020 MSS model [47], which is constructed by multi-source altimeter satellites including HY-2A, Jason-3 and Sentinel-3A. The reference base of the SDUST2020 MSS model is the MSS of Topex/Poseidon +Jason-1+Jason-2+Jason-3 altimetry satellite data for a total of 27 consecutive years from 1993 to 2019. It takes 19 years as a sliding window [48] and covers 80° north and south latitude. The grid resolution is 1'×1.'

E. MEAN DYNAMIC TOPOGRAPHY (MDT) MODEL

The MDT model chosen in this paper is DTU22MDT model [49]. The grid resolution of this model is 7.5.' It is obtained by integrating in situ gravity measurements after differencing the MSS model of DTU21 MSS with XGM2019e geoid model. Among them, the DTU21 MSS model is constructed based on 2Hz altimetry data. Its reference frame is the MSS height of 20 consecutive years of T/P+Jason-

1+Jason-2 altimetry satellite data from 1993 to 2012. It covers a latitude of 90° north and south with a grid resolution of 1'×1' [50].

III. METHODOLOGY

The gravity disturbing potential T at any point on the sphere can be expressed as [5]

$$T = \frac{R}{4\pi} \int_{\sigma} \Delta g S(\psi) d\sigma \tag{1}$$

According to Bruns' formula, the height of the geoid at any point on the sphere can be expressed as

$$N = \frac{T}{\gamma} = \frac{R}{4\pi\gamma} \int_{\sigma} \Delta g(\psi, \alpha) S(\psi) d\sigma \tag{2}$$

where R is the mean radius of the Earth, $\Delta g(\psi, \alpha)$ represents the gravity anomaly on the sphere of radius R, γ represents the average normal gravity of the Earth, α is the spherical azimuth between the calculated point and the variable point, ψ represents the spherical distance between the calculated point and the variable point, $S(\psi)$ is the Stokes kernel function and can be expressed as

$$S(\psi) = \frac{1}{s} - 6s - 4 + 10s^2 - 3(1 - 2s^2)\ln(s + s^2) \tag{3}$$

where $s = \sin(\psi/2)$.

When performing calculations using (2), it is necessary to conduct integration on a global scale. However, due to limitations in computational efficiency and cost, conducting global-scale integration is not feasible. If the integral region is divided into finite sections, such as a few degrees of region, the spherical formula can be transformed into a planar formula. Additionally, by utilizing the FFT method, the time domain integral can be converted into frequency domain convolution to enhance computational efficiency. In eq. (2), we set $d\sigma = \frac{1}{R^2} dxdy$. Eq. (2) is converted to 2D FFT convolution in planar coordinates. The 2D FFT convolution forms in planar coordinates [16] can be formulated as follows

$$N(x, y) = \frac{1}{4\pi\gamma R} F_2^{-1} \{F_2[\Delta g(x, y)] \cdot F_2[S(x, y)]\} \tag{4}$$

where F_2 is the 2D FFT in planar coordinates.

When the distance between the calculation points and the variable point is 0, the kernel function in the formula becomes a singular function. This makes it impossible to calculate the integral value. To solve this problem, a small ball crown with radius s_0 is taken as the center of the calculation point, and this area is called the innermost zone. The geoid height N_s caused by the innermost zone effect can be expressed as

$$N_s = \frac{s_0}{\gamma} \Delta g \tag{5}$$

where $s_0 = \sqrt{\frac{\Delta x \Delta y}{\pi}}$.

IV. RESULTS AND ANALYSIS

A. REMOVE-COMPUTE-RESTORE (RCR)

We validate the algorithm presented in section III. Firstly, we removed the 2159-degree EGM2008 gravity anomaly model from the 2190-degree XGM2019e_2159 gravity anomaly model, the residual gravity anomaly can be derived, the obtained value is input into the 2DFFT convolution (4) and the innermost zone (5) to derive the residual geoid height. Then on the basis of the residual geoid height, the corresponding EGM2008 reference geoid height is recovered, and finally the Stokes formula calculated geoid model is obtained. This model is called Model 1.

The geoid model of XGM2019e_2159 with degree 2190 is referred to as model 2, and the geoid model of EGM2008 with degree 2159 is referred to as model 3. The difference statistics are conducted separately between Model 2 and Model 1, as well as between Model 2 and Model 3. In order to avoid pollution from data with poor accuracy in coastal areas, the difference statistics are rejected by three times of STD, and the results after rejection are shown in Table 1.

TABLE 1. The statistical results of the difference between the geoid heights (unit: m).

Model discrepancy	MAX	MIN	MEAN	STD	Rejection rate
Model 2 - Model 3	0.191	-0.191	0.001	0.044	2.19%
Model 2 - Model 1	0.080	-0.080	-0.001	0.017	2.32%

As can be seen from Table 1, the STD of the geoid height difference between the Model 1 and the Model 2 is 1.7cm, which is 2.7cm less than the STD of the difference between the Model 2 and the Model 3, and Model 1 and Model 2 have a good consistency.

B. THE GEOID MODELING OF THE CHINA SEA AND ITS ADJACENT OCEAN

The RCR technique is employed for geoid modeling in the China Sea and its adjacent ocean. The 2160-degree XGM2019e_2159 reference gravity anomaly model is removed from the marine gravity anomaly model of SDUST2022 GRA, the residual gravity anomaly has been got. Then the residual gravity anomaly is input into 2DFFT convolution (4) and the innermost zone (5) with an integration radius of 1° chosen to acquire the residual geoid height. Subsequently, on the basis of residual geoid height, the corresponding 2160-degree XGM2019e_2159 reference geoid model is restored, ultimately the geoid model of the China Sea and its adjacent ocean is obtained. The information is illustrated in Fig. 2. The geoid model exhibits a maximum value of 76.782m and a minimum value of -23.284m for the China Sea and its adjacent ocean, with statistical results presented in Table 2.

The analysis of Fig. 2 reveals a gradual increase in the oblique state of geoid height from west to east in the China

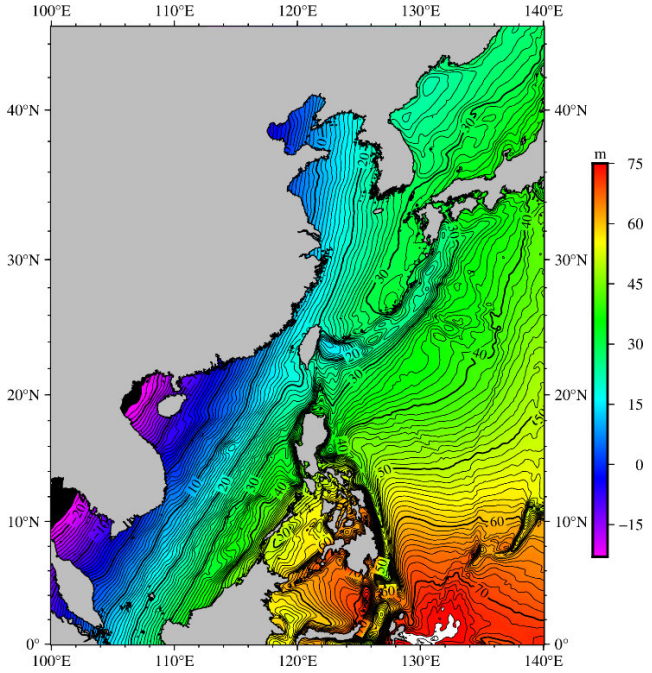

FIGURE 2. Geoid model of China Sea and its adjacent ocean constructed by stokes formula.

TABLE 2. Statistical results of geoid model in China seas and its adjacent ocean (unit: m).

MAX	MIN	MEAN	STD
76.782	-23.284	41.359	17.923

Sea and its adjacent ocean. Specifically, the Beibu Gulf and the Gulf of Thailand exhibit the lowest geoid heights, while near the seamount in the southeast of the Philippine Islands, the highest geoid heights are observed, with a significant difference of up to approximately 100m. Various features of long wavelength and short wavelength of seafloor topography can be seen from the figure. Prominent long-wavelength characteristics encompass trenches, seamounts, basins, and troughs, including notable examples like the Philippine Trench, Palau Trench, Yap Trench and Nankai Trough. The specific detail diagram is shown in the figure 3.

The geoid model in this paper can reflect changes in the seafloor topography. In Figure 3(a), the contour lines illustrate a boat-shaped basin, with the seabed topography representing the Nankai trough. Figures 3(b), (c), and (d) depict the Philippine Trench, Palau Trench, and Yap Trench, respectively. It is evident that there are significant geoid low points near the trenches, with stair-step topography on both sides. Geologically, trenches and troughs are considered the result of the interaction between oceanic and continental plates [53]. Trenches are associated with subduction processes, while troughs are related to seafloor spreading. Additionally, there are discernible short-wavelength features such as small seamounts and shoals.

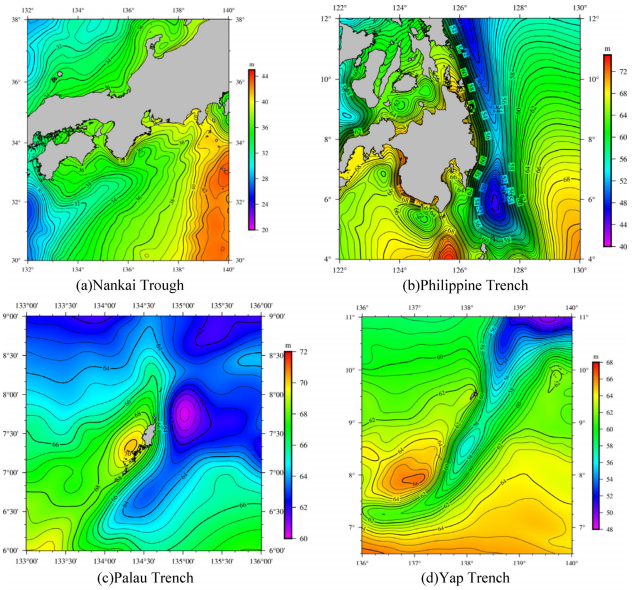

FIGURE 3. Detailed magnification of the geoid model of China Sea and its adjacent ocean constructed by stokes formula at trough and trench.

C. VALIDATION OF GEOID MODELS IN CHINA SEA AND ITS ADJACENT OCEAN

1) COMPARISON WITH THE GEOID CALCULATED BY LSC METHOD

The covariance between gravity anomaly and gravity anomaly, as well as the covariance function between gravity anomaly and geoid, are isotropic [29]. Therefore, we can obtain the covariance table, which includes the covariance between gravity anomaly and gravity anomaly, and the covariance between gravity anomaly and geoid height [28]. Using the RCR technique, the 2160-degree XGM2019e_2159 gravity anomaly model is removed from the SDUST2022 GRA marine gravity anomaly model. Then the residual gravity anomaly is inputted into (A1), and the residual geoid height is calculated using the covariance table. Finally, based on the residual geoid height, the corresponding 2160-degree XGM2019e_2159 reference geoid height is recovered (The specific calculation formula can be found in the Appendix).

The reliability of the geoid model determined by Stokes formula is assessed by analyzing the discrepancy between the Stokes formula constructed geoid model and the LSC method calculated geoid model. The difference distribution is shown in Fig. 4. The three times of STD criterion is employed to exclude data with poor accuracy in coastal areas. The difference statistics after the rejection are shown in Table 3.

TABLE 3. Statistical results of geoid model in China seas and its adjacent ocean (unit: m).

MAX	MIN	MEAN	STD	Rejection rate
0.111	-0.111	-0.002	0.019	1.83%

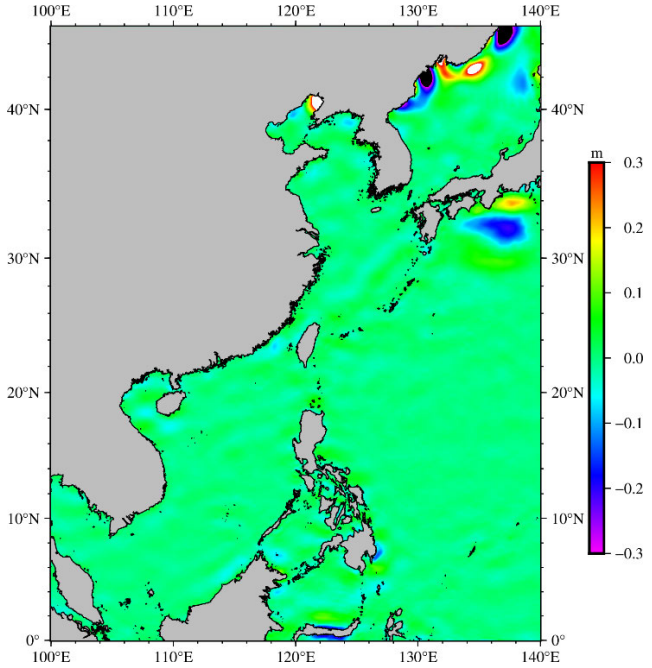

FIGURE 4. Difference distribution of geoid model calculated by stokes formula and LSC method.

According to Table 3, the STD of the difference between the geoid models calculated by the Stokes formula and the LSC method is 1.9cm, which indicates that the geoid models calculated by the two methods are in good agreement on the whole, and the geoid model calculated by the Stokes formula is reliable. The spatial distribution of the comparison between the geoid models computed by the two methods is illustrated in Fig. 4. It can be seen from Fig. 4 that the geoid models calculated by the two methods are relatively consistent in spatial scale, however there are large differences in the Bohai Sea coast, the coast of the Sea of Japan and the eastern ocean of Japan. Particularly significant discrepancies are observed in coastal regions such as the Bohai Sea coast and the coast of the Sea of Japan. To study the impact of the coastline on the geoid height calculated by the two methods, we divided the areas based on the distance from the coastline. Table 4 shows the statistical differences in the geoid models calculated using the two methods in different regions.

TABLE 4. Statistical results of geoid model for different regions of the China seas and its adjacent ocean.

Distance from the coastline（km）	MAX(m)	MIN(m)	MEAN(m)	STD(m)
≤10	0.626	-0.565	0.002	0.061
10~20	0.586	-0.534	0	0.057
20~30	0.588	-0.53	-0.002	0.054
30~40	0.575	-0.53	-0.002	0.054
40~50	0.52	-0.53	-0.002	0.055
>50	0.416	-0.53	-0.002	0.03

According to Table 4, within 50 km of the coastline, there is a obvious difference in the geoid heights constructed by the two methods. This is because the coastline and islands can contaminate the altimetry waveform data, thereby affecting the accuracy of the altimetry data. Consequently, this impacts the precision of gravity anomaly inversion, leading to inaccuracies in the constructed nearshore geoid height model. In offshore areas more than 50 km from the coastline, the geoid models constructed by the two methods are relatively consistent. This indicates that the geoid model developed in this paper using the Stokes formula has a high reliability in open sea regions.

2) COMPARISON OF MDT

The MDT is also computed in order to validate the external reliability of the geoid model calculated using Stokes formula. The geoid model computed calculated by Stokes formula is subtracted from the MSS model of SDUST2020 MSS. A low-pass Gaussian filtering is employed for noise reduction. Ultimately, the MDT with a grid resolution of 1'×1' in the China Sea and its adjacent ocean is obtained. The MDT computed in this study is depicted in Fig. 5. When calculating the MDT, it is essential to standardize the reference ellipsoid and tidal system of both the MSS model and geoid model [54]. The discrepancy resulting from different tidal systems and reference ellipsoids can reach up to 30cm, which cannot be disregarded.

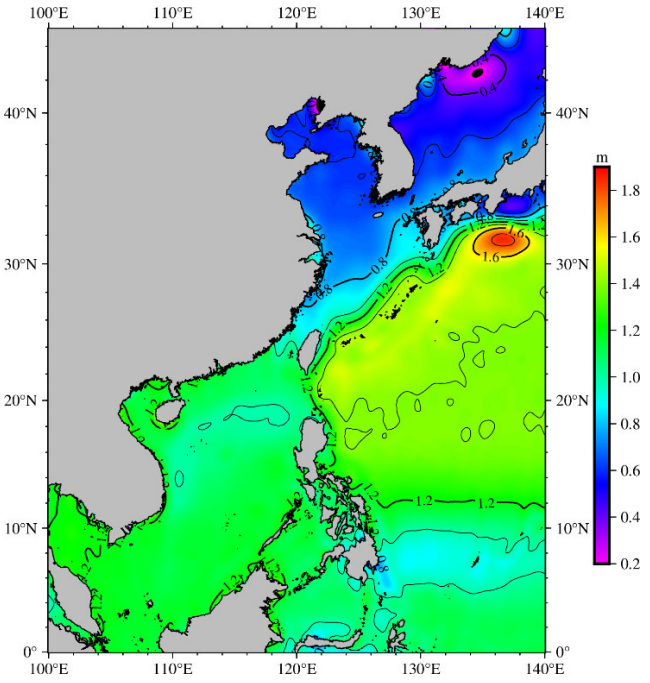

FIGURE 5. MDT model calculated in this paper.

It can be seen from Fig. 5 that the MDT of China Sea and its adjacent ocean areas is positive as a whole, and the MDT from Minjiang Estuary to the north of Japan is relatively low, and its highest point located in the southeast Japan sea area. According to the analysis based on the geostrophic current principle, it is evident that ocean currents are prevalent in regions characterized by high-density sea surface topographic

isolines [55]. Fig. 5 shows the Kuroshio from low latitude to high latitude from Taiwan to southern Japan [44], as well as the mesoscale vortex phenomenon formed by the disturbance of the Kuroshio extension body [56]. In Fig. 5, the larger red area of MDT is located in the southern part of Shikoku and Cape Shionomisaki [57]. There is an anticyclonic vortex in this area, resulting in higher turbulent kinetic energy [58]. Additionally, the influence of the Kuroshio Extension contributes to a greater mixed layer depth here [59]. Consequently, the MDT value in this region is relatively high.

The accuracy of the MDT can be verified by comparing and analyzing it with the DTU22MDT model. The DTU21MSS is based on the average sea surface height over a 20-year period from 1993 to 2012, while the SDUST2020 MSS model is based on the average sea surface height over a 27-year period from 1993 to 2019. Therefore, when comparing these models, it is necessary to deduct the effect of the 7-year sea surface change from the SDUST2020 MSS model. The DTU22MDT is interpolated by bicubic at a resolution of 1'×1,' with the exclusion of points located on islands and land masses. The discrepancy distribution between DTU22MDT and the MDT computed in this study is illustrated in Fig. 6.

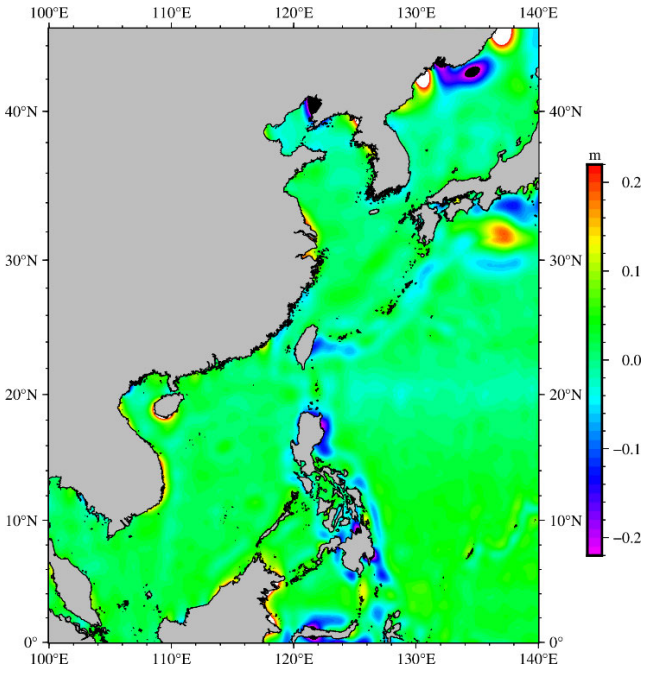

FIGURE 6. Difference distribution between MDT calculated in this paper and the DTU22MDT.

TABLE 5. Statistics of the difference between the MDT calculated in this paper and the DTU22MDT (unit: m).

MAX	MIN	MEAN	STD	Rejection rate
0.114	-0.114	0.010	0.028	2.11%

The difference between the MDT calculated in this paper and the DTU22MDT is statistically analyzed. In order to avoid the interference of poor accuracy data such as coastal areas, the difference results are rejected by three times of STD, and the rejected results are shown in Table 5.

The standard deviation of the two MDT, as shown in Table 5, is calculated to be 2.8cm. This result indicates a high level of agreement between the calculated MDT presented in this paper and that of DTU22MDT as a whole. The differences between the two mean dynamic topographies are primarily observed in coastal regions and the eastern ocean of Japan, as depicted in Fig. 6. In coastal areas, the discrepancies are predominantly attributed to the limited quality of altimetry data. In addition, in the eastern ocean of Japan, the presence of mesoscale vortices generated by disturbances from the Kuroshio extension body leads to heightened kinetic energy within these vortices, consequently resulting in substantial disparities between the two mean dynamic topographies.

V. CONCLUSION

The acquisition of high-precision marine geoid data is essential for the accurate retrieval of seafloor topography and the establishment of a mean dynamic topography. The SDUST2022GRA marine gravity anomaly model is the global marine gravity anomaly model that integrates the inversion of multi-source altimetry satellites, including ICEsat-2 laser satellite for the first time. By utilizing altimetry data from both along-track and cross-track directions, provided by the ICEsat-2 laser satellite. Consequently, it demonstrates a substantial enhancement in terms of both accuracy and spatial resolution. The China Sea and its adjacent ocean are characterized by the Kuroshio Marine movement environment, featuring a complex and dynamic seafloor topography structure. The RCR method is utilized in this paper. The XGM2019e_2159 model of degree 2190 and the EGM2008 model of degree 2159 are used to verify the correctness of Stokes formula. The geoid model of China Sea and its adjacent ocean is constructed based on SDUST2022GRA marine gravity anomaly model employing Stokes formula. The 2D FFT convolution formula in planar coordinate is utilized in the computation.

To verify the reliability of the Stokes formula calculated geoid model, the LSC method is also utilized. The comparison between the geoid model constructed by Stokes formula and the geoid model calculated by LSC demonstrates a high level of spatial consistency, indicating the reliability of the geoid model proposed in this paper. However, there are large differences in the areas with poor quality of coastal altimetry data such as the Bohai Sea coast and the coast of the Sea of Japan. A detailed analysis of the differences between the two geoid models in coastal areas are conducted. The presence of nearshore features and islands has contaminated the altimetric data waveform, resulting in lower accuracy for the coastal geoid models. In the future, we plan to incorporate high-accuracy SWOT satellite data for coastal regions. The SWOT satellite data can further enhance the accuracy and resolution of the inverted gravity anomaly model, allowing

for the construction of a more precise and reliable geoid model.

The MDT model is used to verify the external reliability of the Stokes formula calculated geoid. It can be obtained by utilizing the Stokes formula constructed geoid model combined with the MSS model of SDUST2020 MSS. The MDT reveals the Kuroshio phenomenon, which transfers energy from low to high latitudes as it flows from Taiwan towards the southern coast of Japan. Additionally, the vortex kinetic energy phenomenon caused by the disturbance of the Kuroshio extension body, which makes the background current unstable. The comparative analysis between the MDT and the DTU22MDT model demonstrates a high level of agreement overall, with the exception of areas close to shore where data quality is poor and in the mesoscale vortex region generated by the Kuroshio extension body. This indicates that the calculated MDT presented in this study can be considered reliable. Consequently, it can be seen that the geoid model constructed by Stokes formula in this paper is also reliable.

APPENDIX A
LEAST-SQUARES COLLOCATION

The formula for the LSC method to calculate the residual geoid height from the residual gravity anomaly can be represented as follows [60]

$$N_{res} = C_{N\Delta g}(C_{\Delta g} + D_{\Delta g})^{-1}\Delta g_{res} \tag{A1}$$

where N_{res} is residual geoid height, $C_{N\Delta g}$ represents the covariance matrix of the residual geoid height and residual gravity anomaly, $C_{\Delta g}$ represents the covariance matrix computed between the residual gravity anomaly and itself, $D_{\Delta g}$ is the noise variance matrix of residual gravity anomaly observations, Δg_{res} is residual gravity.

The covariance of the residual quantity in (A1) is primarily composed of two distinct components. The first component is the anomaly error degree variance term that corresponds to the coefficient error of the reference field. The second component is the anomaly degree variance term, which is associated with the residual signal. The covariance $C_{\Delta g\Delta g}$ of the residual gravity anomaly and the covariance $C_{N\Delta g}$ of the residual geoid and the residual gravity anomaly can be expressed as, respectively [61]

$$C_{\Delta g\Delta g} = \sum_{n=2}^{N_{\max}} \delta C_n s^{n+2} P_n(\cos\psi_{PQ}) + \sum_{n=N_{\max}+1}^{\infty} C_n s^{n+2} P_n(\cos\psi_{PQ}) \tag{A2}$$

$$C_{N\Delta g} = \frac{R_B^2}{r_P\gamma_Q}\left[\sum_{n=2}^{N_{\max}} \frac{\delta C_n}{n-1} s^{n+1} P_n(\cos\psi_{PQ}) + \sum_{n=N_{\max}+1}^{\infty} \frac{C_n}{n-1} s^{n+2} P_n(\cos\psi_{PQ})\right] \tag{A3}$$

where $s = \frac{R_B^2}{R^2}$, R_B is the radius of the Bjerhammar ellipsoid, R is the mean radius of the Earth, r_P is the radius of points P, γ_Q is the normal gravity for points Q, ψ_{PQ} is the spherical distance between points P and Q, P_n represents the Legendre polynomial. δC_n is the anomaly error degree variance, which can be expressed as

$$\delta C_n = \left(\frac{GM}{R^2}\right)^2 (n-1)^2 s^{-2(n+2)} \sum_{m=0}^{n} \left(\varepsilon_{Cnm}^2 + \varepsilon_{Snm}^2\right) \tag{A4}$$

C_n is the anomaly degree variance, it can be represented by the Tscherning/Rapp model 4

$$C_n = \frac{A(n-1)}{(n-2)(n+B)} \tag{A5}$$

where $\varepsilon_{C_{nm}}^2$ and $\varepsilon_{S_{nm}}^2$ in (A4) are the variance of the spherical harmonic coefficient of the n degree and the m order of the reference gravitational field, which can be obtained according to the information of the reference gravitational field. The geoid height obtained through the LSC method can be determined by replacing the results of (A2) and (A3) into (A1).

ACKNOWLEDGMENT

The authors would like to express their gratitude to Aviso for providing the altimetry data, the DTU Space Center for sharing the DTU22MDT mean dynamic topography data, and ICGEM for releasing the reference gravity field model data.

REFERENCES

[1] P. Vanicek and N. T. Christou, *Geoid and Its Geophysical Interpretations*. Boca Raton, FL, USA: CRC Press, 1994, pp. 1–30.
[2] R. Tenzer, R. Čunderlík, N. Dayoub, and A. Abdalla, "Application of the BEM approach for a determination of the regional marine geoid model and the mean dynamic topography in the Southwest Pacific Ocean and Tasman Sea," *J. Geodetic Sci.*, vol. 2, no. 1, pp. 8–14, Jan. 2012, doi: 10.2478/v10156-011-0019-6.
[3] Y. H. Wu and Z. C. Luo, "The approach of regional geoid refinement based on combining multi-satellite altimetry observations and heterogeneous gravity data sets," *Chin. J. Geophys.*, vol. 59, no. 5, May 2016, pp. 1596–1607, doi: 10.6038/cjg20160505.
[4] S. Varbla and A. Ellmann, "Iterative data assimilation approach for the refinement of marine geoid models using sea surface height and dynamic topography datasets," *J. Geodesy*, vol. 97, no. 3, p. 24, Mar. 2023, doi: 10.1007/s00190-023-01711-7.
[5] B. Hofmann-Wellenhof and H. Moritz, *Physical Geodesy*, W, H. Freeman, Eds., San Francisco, CA, USA: Springer, 1967, pp. 43–122.
[6] J. Huang and M. Véronneau, "Canadian gravimetric geoid model 2010," *J. Geodesy*, vol. 87, no. 8, pp. 771–790, Aug. 2013, doi: 10.1007/s00190-013-0645-0.
[7] D. T. Vu, S. Bruinsma, and S. Bonvalot, "A high-resolution gravimetric quasigeoid model for Vietnam," *Earth, Planets Space*, vol. 71, no. 1, p. 65, Jun. 2019, doi: 10.1186/s40623-019-1045-3.
[8] K. Matsuo and Y. Kuroishi, "Refinement of a gravimetric geoid model for Japan using GOCE and an updated regional gravity field model," *Earth, Planets Space*, vol. 72, no. 1, p. 33, Mar. 2020, doi: 10.1186/s40623-020-01158-6.
[9] M. Varga, M. Pitoňák, P. Novák, and T. Bašić, "Contribution of GRAV-D airborne gravity to improvement of regional gravimetric geoid modelling in Colorado, USA," *J. Geodesy*, vol. 95, no. 5, p. 53, May 2021, doi: 10.1007/s00190-021-01494-9.
[10] Q. Wu, G. Zhang, B. Wang, L. Zhong, and F. Xiao, "Performance comparison of deterministic and stochastic modifications in Stokes's and Hotine's formulas: The case of Jilin Province, China," *Remote Sens.*, vol. 15, no. 2, p. 376, Jan. 2023, doi: 10.3390/rs15020376.

[11] N. M. Yazid, A. H. M. Din, M. F. Pa'suya, A. H. Omar, N. M. Abdullah, and M. H. Hamden, "The optimization of marine geoid model from altimetry data using least squares Stokes modification approach with additive corrections across Malaysia," *Int. J. Remote Sens.*, pp. 1–27, Nov. 2023, doi: 10.1080/01431161.2023.2268824.

[12] Z. Guan, *Local Gravity Field Approximation Theory and Methods*. Beijing, China: Surveying and Mapping Press, 1997, pp. 20–65.

[13] J. C. Li, J. Y. Chen, J. S. Ning, and D. B. Chao, *Global Gravity Field Approximation Theory Determination 2000 Quasi-Geoid China*. Wuhan, China: Whuhan Univ. Press, 2000.

[14] G. S. van Hees, "Stokes formula using fast Fourier techniques," *Manuscripta Geodaetica*, vol. 15, no. 4, pp. 235–239, Jul. 1990.

[15] C. Hwang, "Inverse Vening Meinesz formula and deflection-geoid formula: Applications to the predictions of gravity and geoid over the South China Sea," *J. Geodesy*, vol. 72, no. 5, pp. 304–312, May 1998, doi: 10.1007/s001900050169.

[16] M. T. Huang, G. J. Zhai, Z. Guan, Y. Ling, and Y. Z. Ouyang, "Comments on FFT technique in spectral geoid determination," *Acta Geodaetica et Cartographica Sinica*, vol. 29, no. 2, pp. 124–131, May 2000, doi: 10.3321/j.issn:1001-1595.2000.02.006.

[17] J. Z. Liu, X. H. Liang, Z. R. Ye, Z. K. Liu, J. J. Lang, and G. C. Wang, "Combining multi-source data to construct full tensor of regional airborne gravity gradient disturbance," *Chin. J. Geophysics*, vol. 63, no. 8, pp. 3131–3143, Aug. 2020, doi: 10.6038/cjg2020O0044.

[18] V. N. Grigoriadis, G. S. Vergos, R. Barzaghi, D. Carrion, and Ö. Koç, "Collocation and FFT-based geoid estimation within the Colorado 1 cm geoid experiment," *J. Geodesy*, vol. 95, no. 5, p. 52, May 2021, doi: 10.1007/s00190-021-01507-7.

[19] L. Cai, X. Wan, H. Hsu, J. Ran, X. Meng, Z. Luo, and Z. Zhou, "The Earth's gravity field recovery using the third invariant of the gravity gradient tensor from GOCE," *Sci. Rep.*, vol. 11, no. 1, p. 3581, Feb. 2021, doi: 10.1038/s41598-021-81840-1.

[20] O. Elghrabawy, "Resolution enhancement of airborne gravity data based on remove–compute–restore scheme (RCR) and downward continuation (DWC) technique," *Geophys. J. Int.*, vol. 231, no. 3, pp. 2034–2047, Sep. 2022, doi: 10.1093/gji/ggac305.

[21] D. A. Natsiopoulos, E. G. Mamagiannou, E. A. Pitenis, G. S. Vergos, and I. N. Tziavos, "GOCE downward continuation to the Earth's surface and improvements to local geoid modeling by FFT and LSC," *Remote Sens.*, vol. 15, no. 4, p. 991, Feb. 2023, doi: 10.3390/rs15040991.

[22] W. E. Featherstone, J. F. Kirby, C. Hirt, M. S. Filmer, S. J. Claessens, N. J. Brown, G. Hu, and G. M. Johnston, "The AUSGeoid09 model of the Australian height datum," *J. Geodesy*, vol. 85, no. 3, pp. 133–150, Mar. 2011, doi: 10.1007/s00190-010-0422-2.

[23] J. Schwabe, H. Ewert, M. Scheinert, and R. Dietrich, "Regional geoid modeling in the area of subglacial Lake Vostok, Antarctica," *J. Geodynamics*, vol. 75, pp. 9–21, Apr. 2014, doi: 10.1016/j.jog.2013.12.002.

[24] C. Hwang, H.-J. Hsu, W. E. Featherstone, C.-C. Cheng, M. Yang, W. Huang, C.-Y. Wang, J.-F. Huang, K.-H. Chen, C.-H. Huang, H. Chen, and W.-Y. Su, "New gravimetric-only and hybrid geoid models of Taiwan for height modernisation, cross-island datum connection and airborne LiDAR mapping," *J. Geodesy*, vol. 94, no. 9, p. 83, Aug. 2020, doi: 10.1007/s00190-020-01412-5.

[25] A. Zaki, M. Magdy, M. Rabah, and A. Saber, "Establishing a marine gravity database around Egypt from satellite altimetry-derived and shipborne gravity data," *Mar. Geodesy*, vol. 45, no. 2, pp. 101–120, Dec. 2021, doi: 10.1080/01490419.2021.2020185.

[26] D. T. Vu, S. Bonvalot, S. Bruinsma, and L. K. Bui, "A local lithospheric structure model for Vietnam derived from a high-resolution gravimetric geoid," *Earth, Planets Space*, vol. 73, no. 1, p. 92, Apr. 2021, doi: 10.1186/s40623-021-01415-2.

[27] H. Al-Ajami, A. Zaki, M. Rabah, and M. El-Ashquer, "A high-resolution gravimetric geoid model for Kuwait using the least-squares collocation," *Frontiers Earth Sci.*, vol. 9, Jan. 2022, Art. no. 753269, doi: 10.3389/feart.2021.753269.

[28] C. Hwang, "A study of the Kuroshio's seasonal variabilities using an altimetric-gravimetric geoid and TOPEX/POSEIDON altimeter data," *J. Geophys. Res., Oceans*, vol. 101, no. 3, pp. 6313–6335, Mar. 1996, doi: 10.1029/95jc03800.

[29] C. C. Tscherning and R. H. Rapp, "Closed covariance expressions for gravity anomalies, geoid undulations, and deflections of the vertical implied by anomaly degree variance models," Dept. Geodetic Sci., Ohio State Univ., Columbus, OH, USA, Tech. Rep. 208, 1974.

[30] N. M. Yazid, A. H. M. Din, K. M. Omar, Z. A. M. Som, A. H. Omar, N. A. Z. Yahaya, and A. Tugi, "Marine geoid undulation assessment over South China Sea using global geopotential models and airborne gravity data," *Int. Arch. Photogramm., Remote Sens. Spatial Inf. Sci.*, vol. 42, pp. 253–263, Sep. 2016, doi: 10.5194/isprs-archives-xlii-4-w1-253-2016.

[31] Y. Liu and L. Lou, "Unified land–ocean quasi-geoid computation from heterogeneous data sets based on radial basis functions," *Remote Sens.*, vol. 14, no. 13, p. 3015, Jun. 2022, doi: 10.3390/rs14133015.

[32] O. B. Andersen, P. Knudsen, and P. A. M. Berry, "The DNSC08GRA global marine gravity field from double retracked satellite altimetry," *J. Geodesy*, vol. 84, no. 3, pp. 191–199, Mar. 2010, doi: 10.1007/s00190-009-0355-9.

[33] L. Stenseng, *Polar Remote Sensing By CryoSat-type Radar Altimetry*. Copenhagen, Denmark: DTU Space, 2011.

[34] S. J. Zhang, T. Y. Jin, Y. H. Chu, and X. X. Kong, "Estimation of the resolution capability of the CryoSat-2 altimeter," *Geomatics Inf. Sci. Wuhan Univ.*, vol. 41, no. 6, pp. 759–764, Jun. 2016, doi: 10.13203/j.whugis20140829.

[35] O. B. Andersen and P. Knudsen, "The DTU17 global marine gravity field: First validation results," *Fiducial Reference Measurements for Altimetry* (International Association of Geodesy Symposia), vol. 150, S. Mertikas and R. Pail, Eds. Berlin, Germany: Springer, Apr. 2019, pp. 83–87, doi: 10.1007/1345_2019_65.

[36] D. T. Sandwell, H. Harper, B. Tozer, and W. H. F. Smith, "Gravity field recovery from geodetic altimeter missions," *Adv. Space Res.*, vol. 68, no. 2, pp. 1059–1072, Jul. 2021, doi: 10.1016/j.asr.2019.09.011.

[37] C. Zhu, J. Guo, J. Gao, X. Liu, C. Hwang, S. Yu, J. Yuan, B. Ji, and B. Guan, "Marine gravity determined from multi-satellite GM/ERM altimeter data over the South China Sea: SCSGA V1.0," *J. Geodesy*, vol. 94, no. 5, p. 50, May 2020, doi: 10.1007/s00190-020-01378-4.

[38] Y. Yu, D. T. Sandwell, S. T. Gille, and A. B. V. Bŏas, "Assessment of ICESat-2 for the recovery of ocean topography," *Geophys. J. Int.*, vol. 226, no. 1, pp. 456–467, Mar. 2021, doi: 10.1093/gji/ggab084.

[39] Z. Li, J. Guo, C. Zhu, X. Liu, C. Hwang, S. Lebedev, X. Chang, A. Soloviev, and H. Sun, "The SDUST2022GRA global marine gravity anomalies recovered from radar and laser altimeter data: Contribution of ICESat-2 laser altimetry," *Earth Syst. Sci. Data*, vol. 16, no. 9, pp. 4119–4135, Sep. 2024, doi: 10.5194/essd-16-4119-2024.

[40] T. Jin, M. Zhou, H. Zhang, J. Li, W. Jiang, S. Zhang, and M. Hu, "Analysis of vertical deflections determined from one cycle of simulated SWOT wide-swath altimeter data," *J. Geodesy*, vol. 96, no. 4, p. 30, Apr. 2022, doi: 10.1007/s00190-022-01619-8.

[41] D. Yu, C. Hwang, O. B. Andersen, E. T. Y. Chang, and L. Gaultier, "Gravity recovery from SWOT altimetry using geoid height and geoid gradient," *Remote Sens. Environ.*, vol. 265, Nov. 2021, Art. no. 112650, doi: 10.1016/j.rse.2021.112650.

[42] K. Wan, S. Xia, J. Cao, J. Sun, and H. Xu, "Deep seismic structure of the northeastern South China Sea: Origin of a high-velocity layer in the lower crust," *J. Geophys. Res., Solid Earth*, vol. 122, no. 4, pp. 2831–2858, Apr. 2017, doi: 10.1002/2016jb013481.

[43] A. Wang, Y. Du, S. Peng, K. Liu, and R. X. Huang, "Deep water characteristics and circulation in the South China Sea," *Deep Sea Res. I, Oceanographic Res. Papers*, vol. 134, pp. 55–63, Apr. 2018, doi: 10.1016/j.dsr.2018.02.003.

[44] M. Latif and T. P. Barnett, "Causes of decadal climate variability over the North Pacific and North America," *Science*, vol. 266, no. 5185, pp. 634–637, Oct. 1994, doi: 10.1126/science.266.5185.634.

[45] P. Zingerle, R. Pail, T. Gruber, and X. Oikonomidou, "The combined global gravity field model XGM2019e," *J. Geodesy*, vol. 94, no. 7, p. 66, Jul. 2020, doi: 10.1007/s00190-020-01398-0.

[46] N. K. Pavlis, S. A. Holmes, S. C. Kenyon, and J. K. Factor, "The development and evaluation of the Earth gravitational model 2008 (EGM2008)," *J. Geophys. Res., Solid Earth*, vol. 117, no. 4, Apr. 2012, Art. no. B04406, doi: 10.1029/2011jb008916.

[47] J. Yuan, J. Guo, C. Zhu, Z. Li, X. Liu, and J. Gao, "SDUST2020 MSS: A global 1' × 1' mean sea surface model determined from multi-satellite altimetry data," *Earth Syst. Sci. Data*, vol. 15, no. 1, pp. 155–169, Jan. 2023, doi: 10.5194/essd-15-155-2023.

[48] J. Yuan, J. Guo, X. Liu, C. Zhu, Y. Niu, Z. Li, B. Ji, and Y. Ouyang, "Mean sea surface model over China seas and its adjacent ocean established with the 19-year moving average method from multi-satellite altimeter data," *Continental Shelf Res.*, vol. 192, Jan. 2020, Art. no. 104009, doi: 10.1016/j.csr.2019.104009.

[49] P. Knudsen, O. Andersen, N. Maximenko, and J. Hafner, "A new combined mean dynamic topography model—DTUUH22MDT," in *Proc. Living Planet Symp.*, 2022, pp. 23–27.
[50] O. B. Andersen, S. K. Rose, A. Abulaitijiang, S. Zhang, and S. Fleury, "The DTU21 global mean sea surface and first evaluation," *Earth Syst. Sci. Data*, vol. 15, no. 9, pp. 4065–4075, Sep. 2023, doi: 10.5194/essd-15-4065-2023.
[51] I. Yasuda, K. Okuda, and Y. Shimizu, "Distribution and modification of North Pacific Intermediate Water in the Kuroshio-Oyashio interfrontal zone," *J. Phys. Oceanogr.*, vol. 26, pp. 448–465, Apr. 1996, doi: 10.1175/1520-0485(1996)026<0448:DAMONP>2.0.CO;2.
[52] T. M. Joyce, I. Yasuda, Y. Hiroe, K. Komatsu, K. Kawasaki, and F. Bahr, "Mixing in the meandering Kuroshio extension and the formation of North Pacific intermediate water," *J. Geophys. Res., Oceans*, vol. 106, no. 3, pp. 4397–4404, Mar. 2001, doi: 10.1029/2000jc000232.
[53] S. Z. Li, X. Z. Ca, G. Z. Wang, B. Liu, X. Y. Li, Y. H. Suo, Z. X. Jiang, L. L. Guo, J. Zhou, P. C. Wang, J. J. Zhu, G. Wang, S. J. Zhao, Y. J. Liu, and G. W. Zhang, "Meso-Cenozoic tectonic evolution and plate reconstruction of the Pacific Plate," *J. Geomechanics*, vol. 25, no. 5, pp. 642–677, Dec. 2019, doi: 10.12090/j.issn.1006-6616.2019.25.05.060.
[54] X. Y. Wan and J. H. Yu, "Mean dynamic topography calculated by GOCE gravity field model and CNES-CLS2010 mean sea surface height," *Chin. J. Geophys.*, vol. 56, no. 6, pp. 1850–1856, Jun. 2013, doi: 10.6038/cjg20130607.
[55] L. F. Peng, W. P. Jiang, T. Y. Jin, and S. J. Zhang, "The global mean dynamic topography and its corresponding sea surface geostrophic current derived from GOCE gravity field model," *Acta Ceanologica Sinica*, vol. 35, no. 2, pp. 15–20, May 2013, doi: 10.3969/j.issn.0253-4193.2013.02.003.
[56] X. Yan, D. Kang, C. Pang, L. Zhang, and H. Liu, "Energetics analysis of the Eddy–Kuroshio interaction East of Taiwan," *J. Phys. Oceanogr.*, vol. 52, no. 4, pp. 647–664, Apr. 2022, doi: 10.1175/jpo-d-21-0198.1.
[57] N. Ebuchi and K. Hanawa, "Influence of mesoscale eddies on variations of the Kuroshio path South of Japan," *J. Oceanogr.*, vol. 59, pp. 25–36, Feb. 2003, doi: 10.1023/A:1022856122033.
[58] W. Sun, C. Dong, R. Wang, Y. Liu, and K. Yu, "Vertical structure anomalies of oceanic eddies in the Kuroshio extension region," *J. Geophys. Res., Oceans*, vol. 122, no. 2, pp. 1476–1496, Feb. 2017, doi: 10.1002/2016jc012226.
[59] J. Yu, B. Gan, Z. Jing, and L. Wu, "Winter extreme mixed layer depth south of the Kuroshio extension," *J. Climate*, vol. 33, no. 24, pp. 10419–10436, Dec. 2020, doi: 10.1175/jcli-d-20-0119.1.
[60] C. Hwang, "Analysis of some systematic errors affecting altimeter-derived sea surface gradient with application to geoid determination over Taiwan," *J. Geodesy*, vol. 71, no. 2, pp. 113–130, Jan. 1997, doi: 10.1007/s001900050080.
[61] C. Zhu, J. Guo, J. Yuan, Z. Li, X. Liu, and J. Gao, "SDUST2021GRA: Global marine gravity anomaly model recovered from Ka-band and Ku-band satellite altimeter data," *Earth Syst. Sci. Data*, vol. 14, no. 10, pp. 4589–4606, Oct. 2022, doi: 10.5194/essd-14-4589-2022.

HUIYING ZHANG is currently pursuing the Ph.D. degree with Shandong University of Science and Technology, Qingdao, China.

Her research interest includes satellite altimetry.

XIN LIU received the Ph.D. degree from Shandong University of Science and Technology, Qingdao, China, in 2007.

She is currently an Associate Professor with the College of Geodesy and Geomatics, Shandong University of Science and Technology. Her research interests include spatial data mining and machine learning.

ZHEN LI is currently pursuing the Ph.D. degree with Shandong University of Science and Technology, Qingdao, China.

His research interest includes marine gravity retrieved from satellite altimetry.

XIAOTAO CHANG received the Ph.D. degree in geodesy and surveying engineering from Wuhan University, Wuhan, China, in 2006.

He is currently a Professor with the Land Satellite Remote Sensing Application Center, MNR, Beijing, China. His research interest includes space geodesy.

HEPING SUN received the Ph.D. degree from the Catholic University of Louvain, Belgium, in 1996.

He is currently an Academician with the Innovation Academy for Precision Measurement Science and Technology, Chinese Academy of Sciences, Wuhan, China. His current research interests include gravity and geodynamics.

HUI LI received the Ph.D. degree from Northwestern Polytechnical University, Xi'an, China, in 2018.

He is currently an Associate Professor with the School of Marine Science and Technology, Xi'an. His research interests include deep ocean sound propagation, array signal processing, and source localization.

JINYUN GUO received the Ph.D. degree from Shandong University of Science and Technology, Qingdao, China, in 2004.

He is currently a Professor with the College of Geodesy and Geomatics, Shandong University of Science and Technology. His research interest includes space geodesy.